Article

Effects of Deep Cryogenic Treatment and Controlled Rolling on Microstructures and Mechanical Properties of an Ultra-High Strength Steel

Yongli Chen [1,2,*], **Xuejiao Zhou [1,2,*]**, **Yuhua Li [2]** and **Fei Tan [2]**

1   The State Key Laboratory for Refractories and Metallurgy, Collaborative Innovation Center for Advanced Steels, International Research Institute for Steel Technology, Hubei Province Key Laboratory of Systems Science in Metallurgical Process, Wuhan University of Science and Technology, Wuhan 430081, China
2   School of Metallurgical and Materials Engineering, Chongqing University of Science and Technology, Chongqing 401331, China
*   Correspondence: hubeichyl@163.com (Y.C.); zxj040203017@126.com (X.Z.)

Abstract: The microstructure mechanisms and mechanical properties of 0.23C-1.96Si-1.94Cr-1.93 Mn-0.35 Mo ultra-high strength steel treated by the deep cryogenic treatment at -196 °C were investigated after the steel was hot rolled at different temperatures. Experimental results show that austenitizing zone rolling with a large reduction in a single pass can comprehensively enhance the mechanical properties due to the high volume of retained austenite and refined lath martensite and bainite. The high strain gradient was suppressed, and tensile strength, yield strength, impact toughness, and total elongation were 2221 MPa, 2017 MPa, 65.5 J, and 16.9%, respectively. In addition, the austenitizing zone rolling can promote the formation of film retained austenite more than dual phase zone rolling, and retained austenite was decreased with an increase in rolling pass in a total rolling reduction of 75%. It is demonstrated that deep cryogenic treatment after austenite zone rolling with a large reduction is the proper method to enhance strength and toughness via refinement strengthening and retained austenite. This work not only reveals that the effects of refinement strengthening and high strain gradients can be markedly improved by deep cryogenic treatment after austenitizing zone rolling with large reduction strategies, but also provides a realistic preparation technology for the exploitation of superior steel applications.

Keywords: deep cryogenic; rolling; ultra-high strength steel; retained austenite; strain gradient; refinement strengthening

1. Introduction

Ultra-high strength steel (UHSS), which has a tensile strength greater than 1000 MPa, is a versatile and superior steel that has been used in various applications, such as wear-resistant parts, high strength anti-collision beams, and aerospace structures [1–3]. Some examples of UHSS include 300 M steel, AerMet 100, Ferrium S53®, S960, and others [4–7]. Traditional UHSS contains a mass alloy of Nb, V, Ti, Cr, Mo, Co, etc. However, this limits the increase in strength and reduces toughness [8–10]. Therefore, the adjustment of the strength and toughness of steel can be achieved by adjusting the microstructure by changing the processes of controlled rolling and controlled cooling and adapting an efficient heat treatment. The latest research indicates that controlled rolling and cooling techniques have important applications in the preparation of UHSS. Li et al. [11] studied the effects of hot rolling and controlled cooling processes on the microstructure and mechanical properties of ultra-high strength steel. Xiong et al. [12] investigated the microstructure and mechanical properties of ultra-high strength steel with a bainitic ferrite/martensite dual-phase structure. Meanwhile, Guo et al. [13] found that different cooling rates have a significant impact on the microstructure and mechanical properties of UHSS. These latest

research results indicate that through controlled rolling and controlled cooling processes, the microstructure and properties of ultra-high strength steel can be modulated, enabling wider applications. In addition, deep cryogenic treatment (DCT) is a new method of improving the mechanical properties of UHSS by cooling it to extremely low temperatures. This technology has been widely researched and applied in the heat treatment of tool and cutter steels. It can increase strength and hardness by lowering the temperature of the steel. However, DCT may also have a significant impact on the microstructure of the steel. Therefore, comprehensive experiments and tests are necessary to ensure its reliability and applicability.

The strength and toughness of UHSS can be enhanced by forming a favorable microstructure, such as lath bainite, lath martensite, retained austenite, and refined grains [14–17]. Refinement strengthening is the most effective method for improving strength and toughness simultaneously, according to the Hall–Petch equation [18]. The combination of bainite and martensite (B/M) also helps improve strength and toughness. Refined lower bainite and lath martensite significantly enhance strength and impact absorption energy [19–21]. Additionally, retained austenite (RA) plays a key role in improving strength and toughness. Film-like RA is more stable than blocky RA and better at hindering the expansion of cracks [22–24]. Rolling is an effective method for improving mechanical properties, particularly through thermomechanical processing (TMCP) [25–27].

However, the rolling temperature is an important factor in improving the mechanical properties of UHSS. While there is a lack of research on UHSS with different starting rolling temperatures and TMCP rolling strategies, recent studies have investigated the mechanical properties and microstructural evolution of UHSS under different processing conditions [28–30]. Further investigation into this area may be worthwhile for the development of UHSS in various applications. Therefore, this paper analyzes the effects of different start rolling temperatures of TMCP and DCT on the microstructure and mechanical properties of UHSS. In addition, the mechanism for the improvement of mechanical properties was analyzed via microstructural characterization.

2. Experimental Materials and Procedures

2.1. Materials and Methods

The UHSS utilized in this experiment was melted in a 65 kg capacity vacuum induction furnace. Table 1 lists the chemical composition as 0.23 C-1.96 Si-1.93 Mn-0.35 Mo. The weight percent (wt.%) of P and S was maintained at a low level in order to minimize any detrimental effects on toughness. The slabs were forged into dimensions of 15 mm × 15 mm × 100 mm (height × width × length) for subsequent rolling experiments. The slabs were then heated in a muffle furnace for 30 min at 1200 °C. Subsequently, the slabs were hot-rolled at temperatures of 970 °C and 880 °C using a Φ350 mm two-roller high-rigidity mill.

Table 1. Chemical composition of steel (wt.%).

C	Si	Mn	Ni	Cr	Mo	P	S	Fe
0.23	1.96	1.93	0.07	1.94	0.35	<0.005	<0.002	margin

The experimental routes are shown in Figure 1 and Table 2. The initial rolling temperatures were set at the austenitizing zone and the $\gamma + \alpha$ dual phases zone. We discuss two different strategies for hot-rolled process: austenitizing zone rolling and dual phases zone rolling. During austenite zone rolling, the microstructure of UHSS is austenitic, while during two-phase zone rolling, it is austenitic + ferritic, resulting in a different rolled microstructure. Due to supercooling phase transition, strain-induced ferritic transition, and compositional segregation, a small amount of ferrite will be generated during the high-temperature zone of austenite. This leads to rolling in the two-phase zone, ultimately causing a decrease in the material's strength and an increase in its toughness, as well

as changes in the ratio of yield strength to tensile strength. Finally, the material's final comprehensive performance is related to factors such as fine grain strengthening, the composition of various microstructures, and crystal orientation, which compete with each other. Therefore, in hot rolling and compression research, it is necessary to study two different rolling strategies: austenite zone rolling and two-phase zone rolling. So, the start rolling temperatures were set as 970 °C (γ, austenitizing zone) and 870 °C (γ + α, dual phases zone), respectively, and the finish rolling temperature fluctuated between 550 °C and 650 °C, measured using the infrared emissivity of 0.95 with a non-contact infrared thermometer of Delixi electric. The steels were first rolled from 15 mm to 3.75 mm at a reduction of 75% with multi-pass rolling in the γ and (γ + α) zone, respectively, then DCT in a cryostat for 30 min when the surface temperature declined to 500 °C, and naturally returned to the room temperature eventually. The DCT after the γ zone rolling and (γ + α) zone rolling was marked as ATR and DPR, respectively.
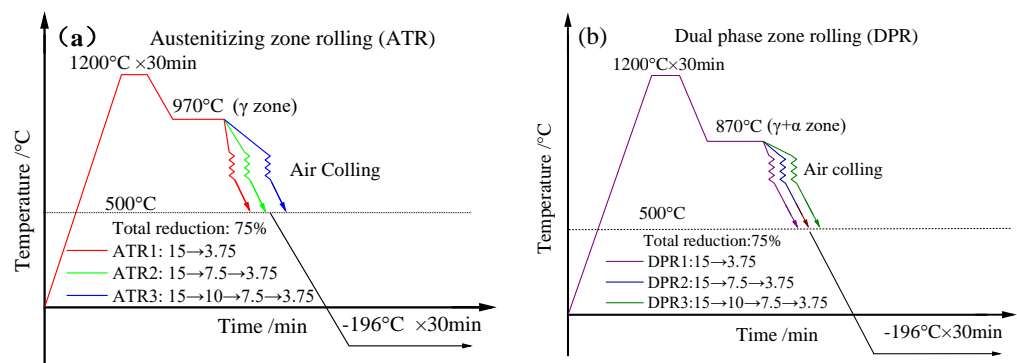
Figure 1. The technical route of TMCP. (**a**) austenitizing zone rolling and DCT, (**b**) dual phase zone rolling and DCT.

Table 2. Mechanical properties of the original steel.

| Rolling Process		Start Rolling Temperature/°C	Rolling Reduction/Mm	DCT
Austenitizing zone rolling (ATR)	ATR1: ATR2: ATR3:	970 °C	15→3.75 15→7.5→3.75 15→10→7.5→3.75	−196 °C × 30 min
Dual phase zone rolling (DPR)	DPR1: DPR2: DPR3:	870 °C	15→3.75 15→7.5→3.75 15→10→7.5→3.75	−196 °C × 30 min

2.2. Mechanical Properties Testing and Microstructural Characterization

Cylindrical specimens for tensile testing and Charpy V-notch impact specimens were prepared according to the material test standards ISO 6892. Tensile experiments were carried out using the WAW-1000 universal tensile machine with a tensile rate of 0.05 mm/s. Microhardness was tested using the WMHV-1000 tester with a test pressure of 10 kg, and the resulting macro Vickers hardness was HV10. To etch the specimens, 4% nital solution was used, and further characterization was performed using a field emission scanning electron microscope (FESEM) (JSM-7800F, Japan). Before testing, the specimens were electrolytically polished for 70 s using a 10% perchloric acid electrolyte with a constant voltage of 25 V. To acquire orientation information, the electropolished specimens were tested using electron backscatter diffraction (EBSD) with a scanning voltage of 20 kV and a step size of 0.15 μm, using the Oxford symmetry system. Crystal orientation, grain size, and texture components were finally analyzed using the HKL-Channel 5 software.

3. Results and Discussions

3.1. Microstructure and Mechanical Properties of the Original Steel

Figure 2a presents the microstructure of the original steel, which mainly consists of lath martensite (LM) and bainite (B). Figure 2b shows that crystal orientation is dominantly focused on [111], with less orientation towards [001]. Figure 2c,d reveals that the steel comprises a large proportion at 59.2% of low angle grain boundaries (LABs), with GB values ranging from 2° to 15°. This is due to the generation of low ratio recrystallization grains during the rolling deformation process. The average grain size is 14.6 μm^2, with most of the grains having a diameter below 20 μm^2, and a relatively low proportion of grains above 22 μm^2. Table 3 lists the mechanical properties of the original steel, including its tensile strength (TS), yield strength (YS), Vickers hardness (VH), and total elongation (TEL), which are 1743 MPa, 1385 MPa, 300 HV, and 13.8%, respectively.
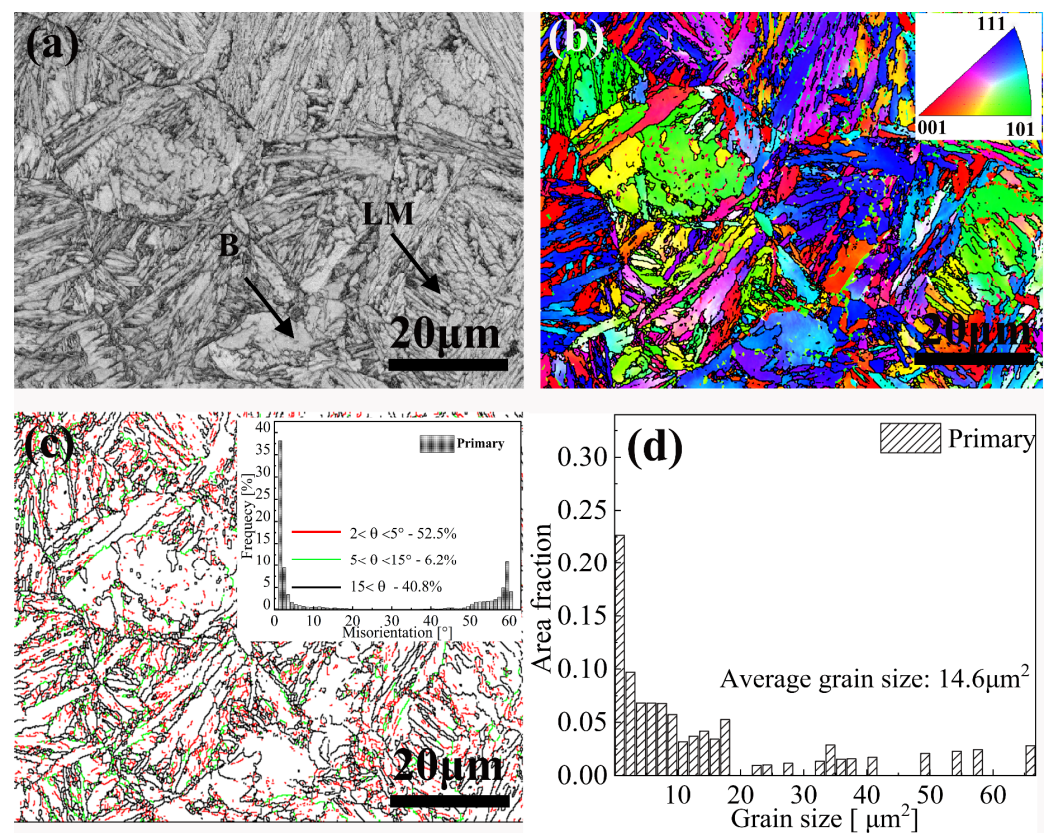
Figure 2. Microstructure of no-treated steel. (**a**) band contrast map, (**b**) invert polar figure, (**c**) low/high angle grain boundary, (**d**) grain size.

Table 3. Mechanical properties of original steel.

Properties	TS/MPa	YS/MPa	HV/Kgf/mm^2	TEL/%
Values	1743	1385	300	13.8

3.2. The Mechanical Properties of DCT Steel

In Figure 3, we can see the mechanical properties of processed steel. The yield strength (YS) was measured using the 0.2% offset method. Compared to the original non-tread (NT) steel, the tensile strength (TS), yield strength (YS), Vickers hardness (VH), and total elongation (TEL) were increased by 15.1%, 8.5%, 3.7%, and 3.6%, respectively. Based on Figure 3c, it was observed that, in general, the higher the single pass reduction during hot rolling, the higher the yield strength and tensile strength ratio of the material during subsequent deep cold treatment, regardless of whether ATR or DPR processing condi-

tions were used. As the number of pass reductions increased, the yield-to-tensile ratio under both processing conditions decreased. A careful comparison between ATR and DPR conditions indicated that the change in yield-to-tensile strength ratio was more gradual (0.88–0.084) under DPR processing conditions, while the decrease in ATR was more significant (0.91–0.75). This may have been due to the fact that, under ATR conditions, dislocations formed by rolling deformation recovered at high temperatures, resulting in a larger overall grain size of the material and a decrease in its yield-to-tensile strength ratio. However, under DPR processing conditions in the two-phase region rolling, the generation of strain-induced ferrite and the formation of more internal dislocations through rolling deformation resulted in a relatively high and stable yield-to-tensile strength ratio, as the recovery temperature was relatively lower than that under ATR and the recovery effect was poor. This represents a significant improvement in TS/YS without sacrificing TEL. The TS, YS, and TEL decreased gradually with an increase in rolling reduction with multi-pass. When the starting rolling temperature was 970 °C, they showed a decreasing trend, while they showed the opposite trend when the starting rolling temperature was 870 °C. ATR1 achieved the maximum improvement in TS and TEL simultaneously, with TS, YS, impact energy, and TEL at 2221 MPa, 2017 MPa, 65.5 J, and 16.9%, respectively. Therefore, we can conclude that ATR is beneficial for strengthening UHSS and provides significant technical guidance and support for producing UHSS.
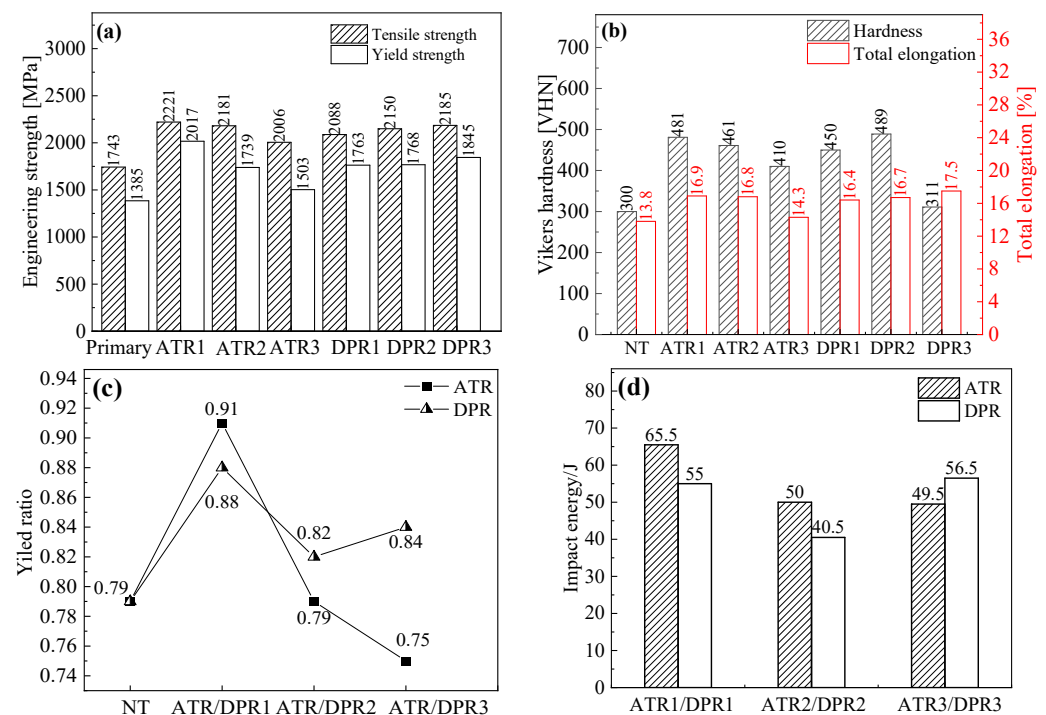

Figure 3. Mechanical properties. (**a**) tensile strength and yield strength, (**b**) hardness and total elongation, (**c**) yield ratio, (**d**) Charpy impact absorption energy at room temperature.

3.3. The Evolution of Microstructure under the Different Starting Rolling Temperatures

As shown in the SEM images presented in Figure 4, the microstructure of the different starting rolling temperatures consisted of grain boundaries, lath boundaries, and retained austenite. In the secondary electron imaging process of SEM, the contrast of SEM was due to the absorption and reflection of secondary electrons by the material surface height and composition. Since the plate martensite LM was in the form of plates, and the bainite was in the form of intragranular nodules, they could be directly identified from SEM. RA was distributed in the form of a thin film at the grain boundary due to its high carbon content, and due to its high electron scattering, it has a high contrast, appearing as a thin film and brighter state. The ATR1-3 microstructure was composed of lath martensite (LM),

massive bainite (MB), and retained austenite (RA), while the DPR 1-3 microstructures contained LM, MB, RA, and ferrite (F). Comparing the microstructure under ATR and DPR, the LM under ATR had a wider lath width, while DPR was shorter and thinner. Notably, there was a significant increase in the refinement of LM with the increase of rolling reduction. Additionally, the volume of MB under DPR was relatively larger than ATR. The SEM images also showed a visible difference between the RA films. Combining the SEM images with the volume fraction of RA in Figure 4g, the volume fraction of RA under ATR was significantly greater than DPR. Furthermore, the fraction of RA decreased with the increase of rolling reduction. This indicates that rolling at the γ zone (970 °C) promotes the formation of RA and its volume is negatively correlated with rolling reduction.
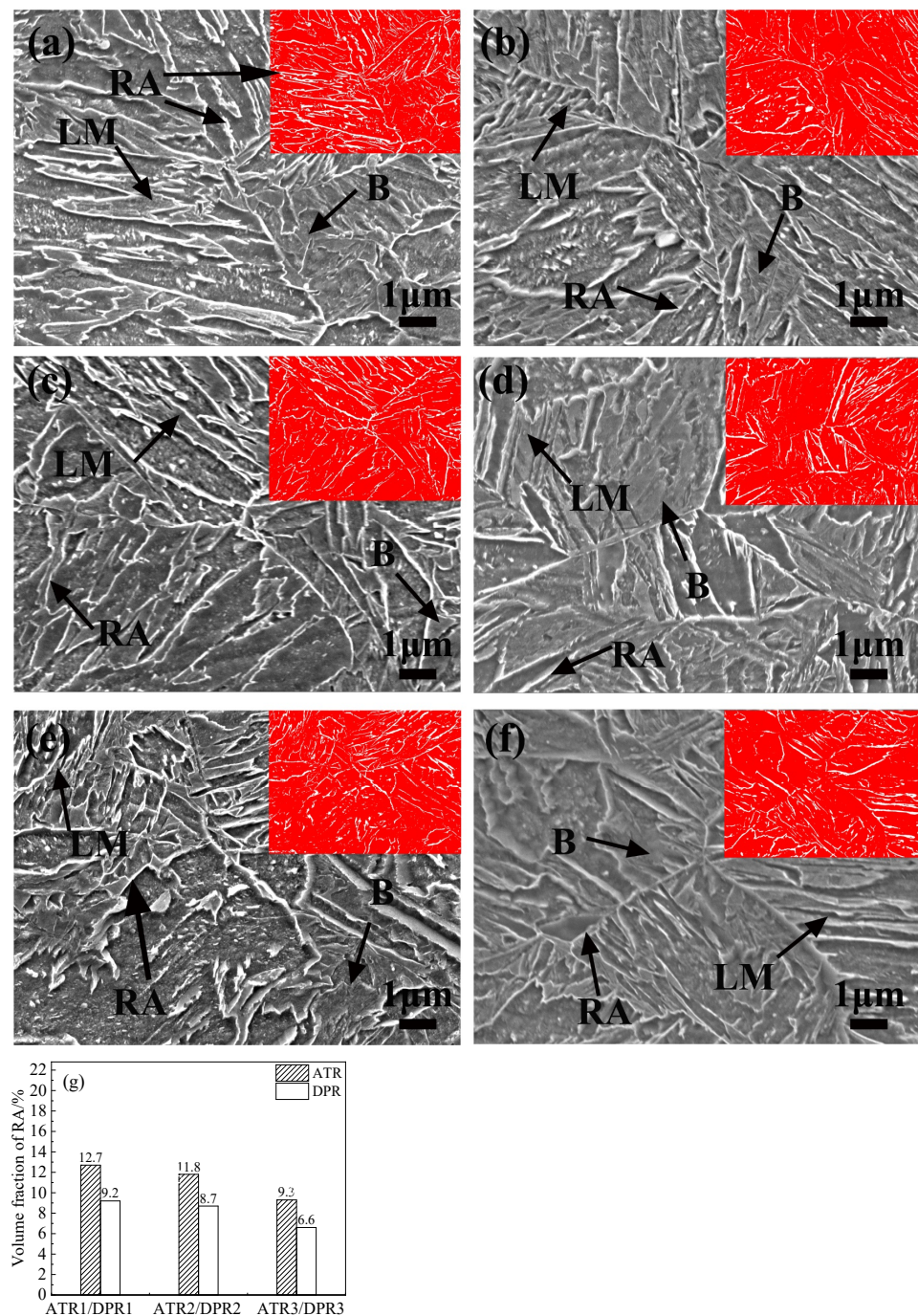
Figure 4. The SEM images under corresponding parameters. (**a**) ATR1, (**b**) DPR1, (**c**) ATR2, (**d**) DPR2, (**e**) ATR3, (**f**) DPR3, (**g**) the volume fraction of retained austenite.

3.4. Effect of Star Rolling Temperature on the Fracture Behavior

Fractures in materials are a sign of ageing and failure, making the study of fracture behavior highly important. To prevent such failure, it is essential to have a comprehensive understanding of the microstructure morphologies of steels. This understanding is especially important in industries where failure can result in serious accidents. In this study, the SEM was used to observe the microstructure morphologies of the steels, which are shown in Figure 5. Additionally, the Charpy impact absorption energy under different parameters was analyzed, and the results are presented in Figure 3d. These results indicate that there are differences in the impact absorption energy depending on the parameters used. The values observed were 65.5 J, 50 J, and 49.5 J in ATR1-3, and 55 J, 40.5 J, and 56.5 J in DPR1-3, respectively. These findings highlight the need for further research in this area and suggest that additional studies could help to refine our understanding of fracture behavior and improve the safety of industrial materials and structures.
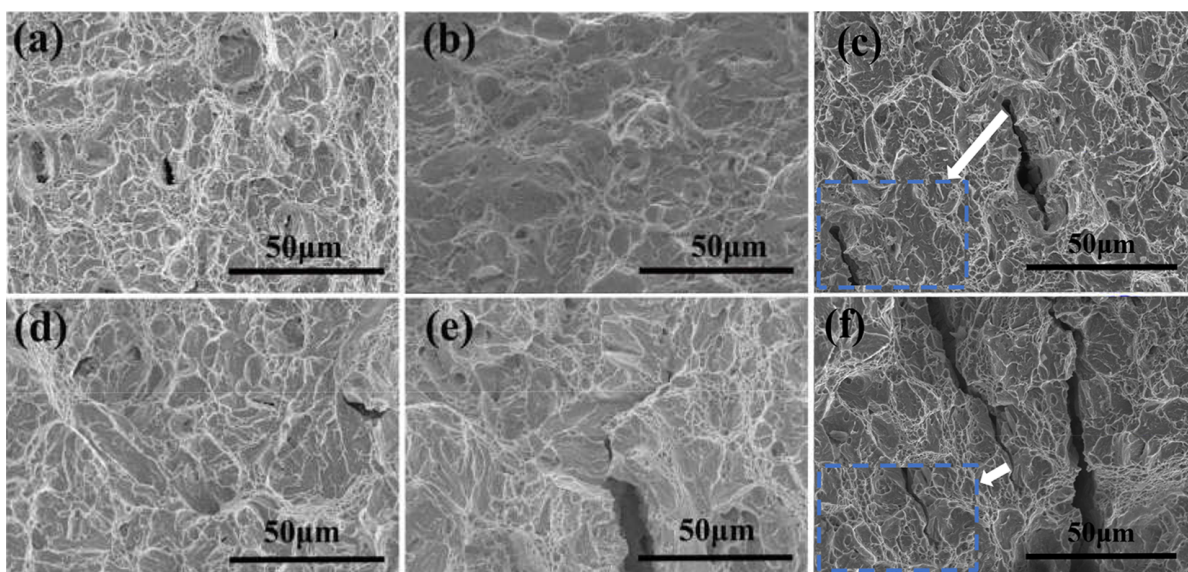

Figure 5. The SEM fracture of treated steels at room temperature. (**a**) ATR1, (**b**) ATR2, (**c**) ATR3 and partial enlargement, (**d**) DPR1, (**e**) DPR2, (**f**) DPR3 and partial enlargement.

The fracture morphology indicates that the treated steel underwent ductile fracture, as evidenced by the numerous tearing dimples present, along with the snake slip located on the inner wall of the dimples. Furthermore, the size of the dimples in ATR was larger than in DPR. Additionally, no significant cracks were observed under ATR during the increase of rolling pass, whereas the length of the crack expanded with the increase of rolling pass under DPR. The cracks observed in both ATR and DPR were transcrystalline and intercrystalline, as shown in the enlarged image (blue dotted circle) in Figure 5c,d. Thus, it can be inferred that ATR can more effectively promote the enhancement of toughness than DPR.

3.5. The Evolution of the Prior Austenite Grain Boundary

Figure 6 is analyzed based on crystal orientation difference and grain rotation, mainly analyzing the influence of prior austenite grains under compression deformation. The prior austenite grain size has a significant effect on the strength and toughness of high strength steel. In steel production, the size of child grains depends on the size of prior austenite grains, which are formed during the austenitization process. When prior austenite grain size is larger, fewer nucleation sites are available during cooling, resulting in larger child grains. Conversely, smaller prior austenite grains create more nucleation sites and smaller child grains. Thus, the size of prior austenite grains directly affects the size of child grains, which impacts the microstructure and mechanical properties of steel. By carefully controlling prior austenite grain size, it is possible to achieve the desired material properties

for specific applications. In addition, the Hall–Petch equation elucidates the relationship between grain size and strength. It shows that decreasing the grain size can achieve the elevation of strength and toughness simultaneously via increasing the density of the grain boundary and hindering the movement of dislocation.
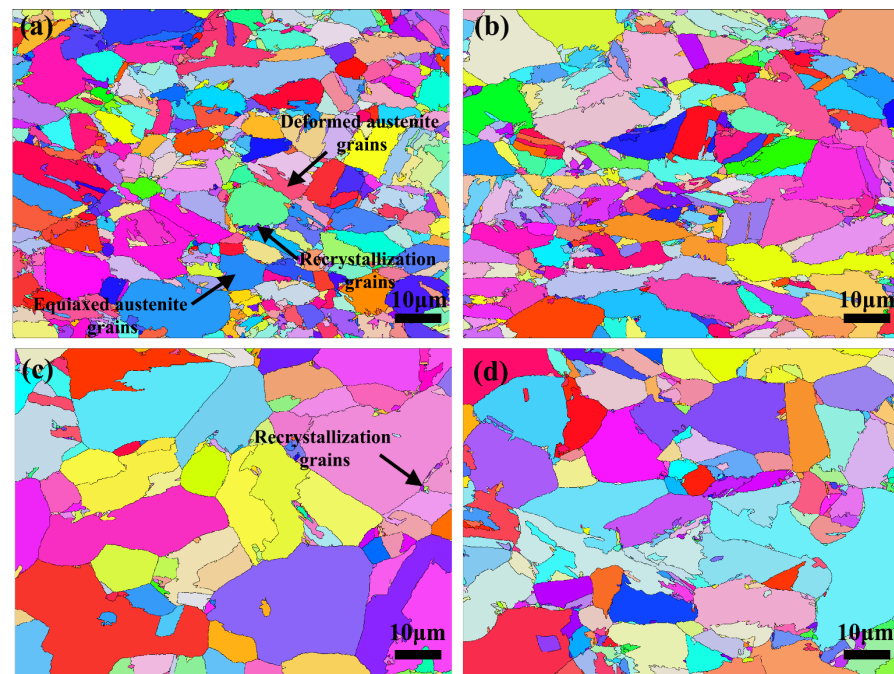

Figure 6. The prior austenite grains under corresponding treatments. (**a**) ATR1, (**b**) ATR3, (**c**) DPR1, (**d**) DPR3.

However, the size of child grains is influenced by the size of prior austenite grains. This section analyzed the evolution of prior austenite grains by reconstructing EBSD data. As shown in Figure 6, the reconstructed prior austenite grains for ATR1, ATR3, DPR1, and DPR3 are presented. Under ATR1, many fine prior austenite grains were observed, with more fine grains nucleated from prior austenite grain boundaries (PAGs). The PAGs were divided into even finer grains. On the other hand, under ATR3, the nucleation of PAGs weakened significantly with an increase in rolling pass, and the average size of PAGs in ATR3 was smaller than in ATR1. In contrast to the PAGs of ATR, there was no obvious recrystallization in DPR. Most of the PAGs were deformed grains, and some PAGs were divided during the DPR treatment. With an increase in rolling pass, some PAGs were eventually divided into two parts in DPR3. Therefore, it can be deduced that large reduction rolling at the γ zone of 970 °C more easily promotes the occurrence of dynamic recrystallization. The large reduction rolling at (γ + α) zone of 870 °C has a weak effect on the activation of dynamic recrystallization. From the combination of the Hall–Petch relationship and dislocation theory, it can be concluded that more grain boundaries lead to improved strength and toughness. The child grain will be finer due to the fine parent grain (PAGs). Therefore, the mechanical properties such as tensile strength (TS), total elongation (TEL), and impact absorption energy in ATR1 were better than those in DPR1.

3.6. The Evolution of Local Misorientation

Impact energy is a representation of steel toughness. However, the sensitivity of the microstructure directly affects the steel's ability to resist impact. Treated steel typically retains stress from the processing, which leads to the formation of a strain gradient. An excessive strain gradient affects the stability of the microstructure and can induce the occurrence of microcracks [31]. To analyze the strain gradient, the Channel 5 program was used to measure the local misorientation relationship. In Figure 7, we can see the

local misorientation map (KAM) and the distribution relative frequency. From Figure 7a,b, we can infer that there are more regions in ATR with a misorientation ranging from 3–5°, which are indicated by red and yellow colors. Additionally, it is evident that ATR1 has more such regions than ATR3. These findings suggest that there is a higher probability of microcracks occurring in these regions, with the most high strain gradient zones being located in the LM region. On the other hand, the low strain gradient zone was mainly focused on the B region. It is also worth noting that the high strain gradient zone decreased as the rolling pass increased, as shown in Figure 7b. This implies that the possibility of local microcrack formation increased, leading to a decrease in the impact toughness. Furthermore, we can observe from Figure 7e that DPR has a lower strain gradient than ATR, which is also supported by the available data. This indicates that the possibility of microcrack formation in ATR was higher than that in DPR, and hence, the impact toughness and tensile strength in DPR should be better than ATR. It is interesting to note, however, that the macro impact absorption energy presented an opposite result. Overall, these findings suggest that the strength-toughness variation is affected by several factors, including the misorientation map, strain gradient, and microcrack formation probability. Therefore, it is important to take these factors into consideration while designing materials and assessing their properties.
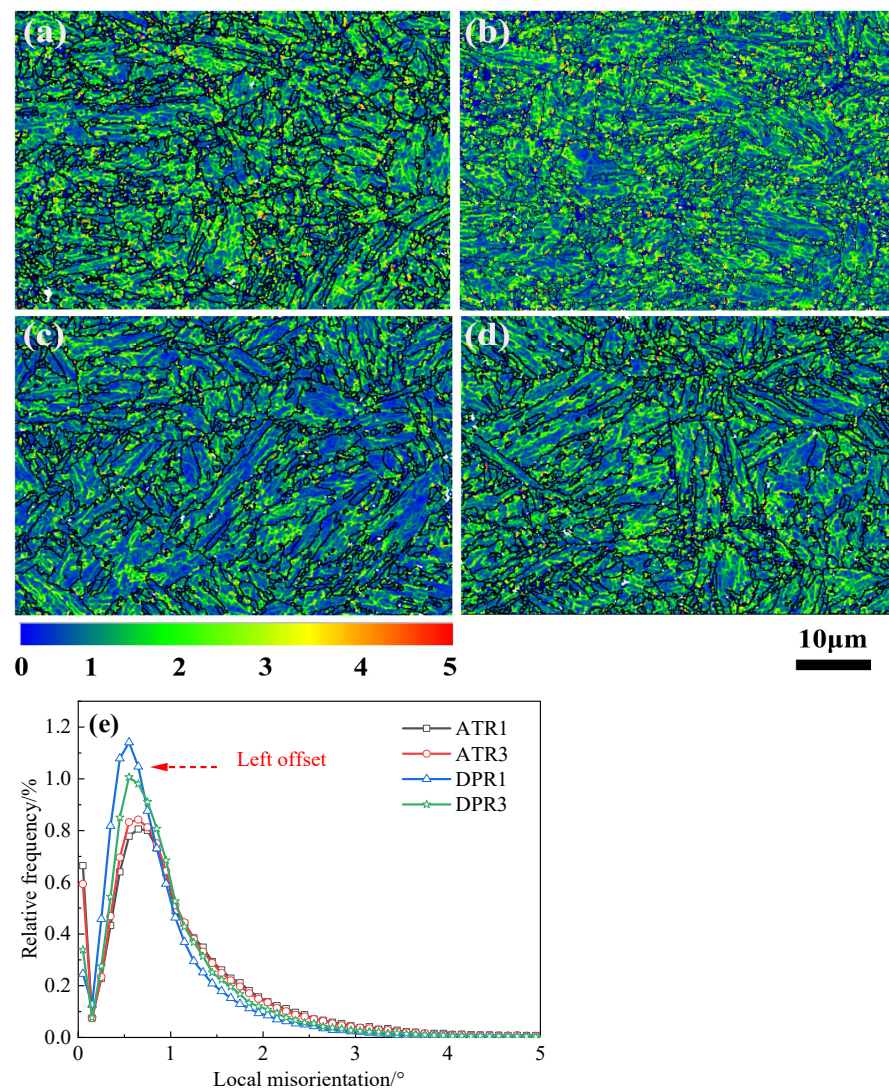
Figure 7. KAM in corresponding parameters. (**a**) ATR1, (**b**) ATR3, (**c**) DPR1, (**d**) DPR3, (**e**) the relative frequency of local misorientation, the rainbow legend bar shows the corresponding angle zone of KAM map.

3.7. The Interaction of Martensite and Bainite Transformation

B and M are important microstructures that affect the strength and toughness of high strength steel. As we know, Kikuchi patterns may have a lower intensity due to differences in lattice imperfections of B/M. Since B has a higher quality Kikuchi pattern than M, the band contrast (BC) value of M will be weaker than that of B [32]. Using the BC maps from EBSD data, the volume fraction and distribution of B/M were extracted and are listed in Figure 8. In ATR and DPR, the volume fraction of M was greater than that of B and exceeded 50%. The microstructure in ATR and DPR is a complex mix of LM, LB, and some blocky bainite (BB). Short LB, short LM, and BB accounted for a large proportion, and a lower proportion of long LB in a PAGs under the ATR1, 3. In contrast, long LB accounted for a large proportion in a PAGs under the DPR1, 3. The average size of B/M in ATR is lower than that in DPR due to the size of PAGs, as shown in Figure 6. The Coarsening of LB and LM is suppressed due to the refinement of PAGs size, and the increases of RA, refined BB, and decreases in coalescent B would benefit the improvement of strength and toughness [33,34]. Therefore, combined with the mechanical properties, Figure 8 shows that there are more refined LB, BB, and LM in ATR than in DPR. The coalescent B is also reduced in the DPR. The size of PAGs directly affects the size of B/M, and the transformation of B will be weakened in the ATR with the increase of rolling pass and strengthened in the DPR with the increase of rolling pass. However, the transformation of M is located in the main stage in ATR and DPR. The volume fraction of B/M is slightly different, with M and B in the range of 56.8~59.6% and 40.4~43.2%, respectively. It can be inferred that decreasing the PAGs and refining the BB in the ATR is more beneficial than in the DPR for improving the strength and toughness of the steel.
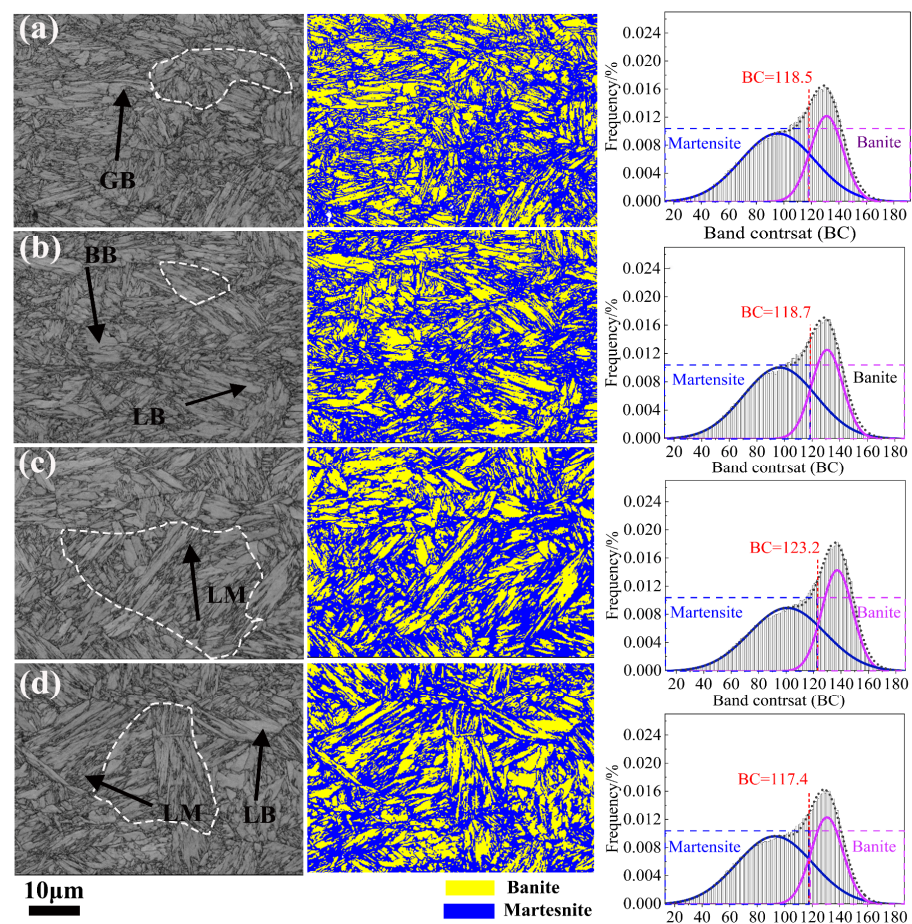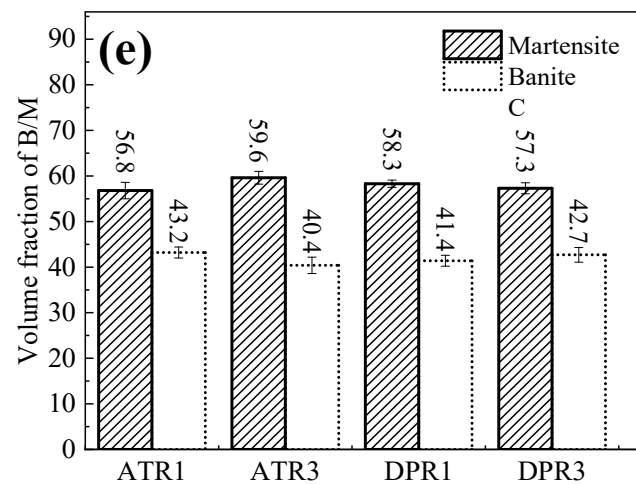

Figure 8. *Cont.*

Figure 8. The distribution of bainite and martensite based on the EBSD data. (**a**) ATR1, (**b**) ATR3, (**c**) DPR1, (**d**) DPR3, (**e**) the volume fraction of B/M and the band contrast map (BC) on the left, phase map in the middle, and frequency distribution fitting graph (Gaussian) of BC on the right.

Based on the information presented, it can be concluded that the strength-toughness of treated steel is influenced by various factors that produce different mechanical properties. As shown in Figure 3, ATR1 exhibited better TS, YS, and impact absorption energy than DPR1. It was observed that the mechanical properties of ATR3 and DPR3 were affected by the increase in rolling passes. The difference in mechanical properties can be attributed to the issue of strengthening the coordination of mechanisms, which can be explained by microstructural characterization. Figure 4 illustrates the distribution and quantitative expression of RA. The volume fraction of RA was higher in ATR1,3 compared to DPR1,3, and the volume fraction decreased with rolling pass in the same total reduction. The volume fraction of RA was 12.7%/9.9% and 9.3%/6.6% in ATR1/DPR1 and ATR3/DPR3, respectively. Film-like RA was observed to be superior to blocky RA in terms of impact toughness. Moreover, PAGs in Figure 6 show that ATR is more effective in refining PAGs than DPR, resulting in the formation of refined child grains. As per the Hall–Petch equation, refinement strengthening has a more significant impact in ATR than DPR. The strengthening effect of fine grain strengthening and retained austenite mitigates the influence of excessive strain gradient, which is why the mechanical properties of ATR1 exceeded those of DPR1. Furthermore, even though DPR has low refinement strengthening, the low strain gradient enhances plasticity by reducing the sensitivity of the microstructure and decreasing the probability of microcrack formation. Therefore, there is more TEL in DPR than ATR.

4. Conclusions

The DCT and TMCP were utilized to exploit the evolution of the mechanical properties and microstructure of 0.23C-1.96Si-1.94Cr-1.93 Mn-0.35 Mo UHSS. Innovation and practicality conclusions were listed as follows:

(1) The ATR1 with a large reduction realized the maximum strength-toughness, and the TS, YS, TEL, and impact energy were 2221 MPa, 2017 MPa, 65.5 J, and 16.9%, respectively. This shows that the large reduction rolling in 970 °C in γ zone is beneficial to the maximum optimization of strength-toughness.

(2) According to the division of the B/M phase map, the B and M are the main microstructures during ATR and DPR, there is more refined LM, BB, LB, and no excessive coalescent B in ATR, and the improvement of strength-toughness would be better than in DPR.

(3) ATR will enhance the strain gradient of local misorientation, the refinement strengthening, and the existence of high-volume fraction film-like RA, and it can effectively compensate for the adverse effects of excessively high strain gradients.

Abbreviations and Notations List

ATR	Austenitizing zone rolling
B	Bainite
DCT	Deep cryogenic treatment
DPR	Dual phase zone rolling
EBSD	Electron backscatter diffraction
F	Ferrite
FESEM	Field emission scanning electron microscope
LM	Lath martensite
KAM	Local misorientation map
LABs	Low angle grain boundaries
M	Martensite
PAGs	Prior austenite grain boundaries
RA	Retained austenite
TS	Tensile strength
TMCP	Thermomechanical processing
TEL	Total elongation
UHSS	Ultra-high strength steel
VH	Vickers hardness
YS	Yield strength

References

1. Merklein, M.; Lechler, J.; Geiger, M. Characterisation of the flow properties of the quenchenable ultra high strength steel 22MnB5. *CIRP Ann.* **2006**, *55*, 229–232. [CrossRef]
2. Etterdal, B.; Askheim, D.; Grigorian, H.; Gladsø, R. Strengthening of offshore steel components using high-strength grout: Component testing and analytical methods. In Proceedings of the Offshore Technology Conference, Houston, TX, USA, 30 April–3 May 2001.
3. Da Sun, S.; Liu, Q.; Brandt, M.; Luzin, V.; Cottam, R.; Janardhana, M.; Clark, G. Effect of laser clad repair on the fatigue behaviour of ultra-high strength AISI 4340 steel. *Mater. Sci. Eng. A* **2014**, *606*, 46–57. [CrossRef]
4. Zhong, J.-Y.; Sun, M.; Liu, D.-B.; Li, X.-G.; Liu, T.-Q. Effects of chromium on the corrosion and electrochemical behaviors of ultra high strength steels. *Int. J. Miner. Metall. Mater.* **2010**, *17*, 282–289. [CrossRef]
5. Zhang, Y.; Zhan, D.; Qi, X.; Jiang, Z. Effect of solid-solution temperature on the microstructure and properties of ultra-high-strength ferrium S53® steel. *Mater. Sci. Eng. A Struct. Mater. Prop. Microstruct. Process.* **2018**, *730*, 41–49. [CrossRef]
6. Barsanti, M.; Beghini, M.; Frasconi, F.; Ishak, R.; Monelli, B.D.; Valentini, R. Experimental study of hydrogen embrittlement in Maraging steels. *Procedia Struct. Integr.* **2018**, *8*, 501–508. [CrossRef]
7. Wang, F.; Zhao, O.; Young, B. Flexural behaviour and strengths of press-braked S960 ultra-high strength steel channel section beams. *Eng. Struct.* **2019**, *200*, 109735. [CrossRef]
8. Vogl, V.; Åhman, M.; Nilsson, L.J. The making of green steel in the EU: A policy evaluation for the early commercialization phase. *Clim. Policy* **2021**, *21*, 78–92. [CrossRef]
9. Olofsson, E. Regional effects of a green steel industry–fuel substitution and feedstock competition. *Scand. J. For. Res.* **2019**, *34*, 39–52. [CrossRef]
10. Nassiraei, H. Probability distribution models for the ultimate strength of tubular T/Y-joints reinforced with collar plates at room and different fire conditions. *Ocean. Eng.* **2023**, *270*, 113557. [CrossRef]
11. Miao, S.; Xie, Z.; Lin, Y.; Fang, Q.; Tan, J.; Zhao, Y. Mechanical Properties, Thermal Stability and Microstructures of W-Re-ZrC Alloys Fabricated by Spark Plasma Sintering. *Metals* **2020**, *10*, 277. [CrossRef]

12. Xiong, Z.P.; Kostryzhev, A.G.; Stanford, N.E.; Pereloma, E.V. Microstructures and mechanical properties of dual phase steel produced by laboratory simulated strip casting. *Mater. Des.* **2015**, *88*, 537–549. [CrossRef]

13. Guo, X.; Liu, S.; Xu, J.; Wang, S.; Fu, L.; Chai, Z.; Lu, H. Effect of step cooling process on microstructures and mechanical properties in thermal simulated CGHAZ of an ultra-high strength steel. *Mater. Sci. Eng. A* **2021**, *824*, 141827. [CrossRef]

14. Lan, H.; Du, L.; Li, Q.; Qiu, C.; Li, J.; Misra, R. Improvement of strength-toughness combination in austempered low carbon bainitic steel: The key role of refining prior austenite grain size. *J. Alloys Compd.* **2017**, *710*, 702–710. [CrossRef]

15. Zou, Y.; Xu, Y.; Hu, Z.; Chen, S.; Han, D.; Misra, R.; Wang, G. High strength-toughness combination of a low-carbon medium-manganese steel plate with laminated microstructure and retained austenite. *Mater. Sci. Eng. A* **2017**, *707*, 270–279. [CrossRef]

16. Wu, S.; Wang, D.; Di, X.; Li, C.; Zhang, Z.; Zhou, Z.; Liu, X. Strength-toughness improvement of martensite-austenite dual phase deposited metals after austenite reversed treatment with short holding time. *Mater. Sci. Eng. A* **2019**, *755*, 57–65. [CrossRef]

17. Luo, H.; Wang, X.; Liu, Z.; Yang, Z. Influence of refined hierarchical martensitic microstructures on yield strength and impact toughness of ultra-high strength stainless steel. *J. Mater. Sci. Technol.* **2020**, *51*, 130–136. [CrossRef]

18. Weertman, J. Hall-Petch strengthening in nanocrystalline metals. *Mater. Sci. Eng. A* **1993**, *166*, 161–167. [CrossRef]

19. Pavlina, E.; Van Tyne, C. Correlation of yield strength and tensile strength with hardness for steels. *J. Mater. Eng. Perform.* **2008**, *17*, 888–893. [CrossRef]

20. Chakraborty, J.; Chattopadhyay, P.; Bhattacharjee, D.; Manna, I. Microstructural refinement of bainite and martensite for enhanced strength and toughness in high-carbon low-alloy steel. *Metall. Mater. Trans. A* **2010**, *41*, 2871–2879. [CrossRef]

21. Lu, X.; Qian, D.; Li, W.; Jin, X. Enhanced toughness of bearing steel by combining prior cold deformation with martensite pre-quenching and bainite transformation. *Mater. Lett.* **2019**, *234*, 5–8. [CrossRef]

22. Zhao, P.; Zhang, B.; Cheng, C.; Misra, R.K.; Gao, G.; Bai, B.; Weng, Y. The significance of ultrafine film-like retained austenite in governing very high cycle fatigue behavior in an ultrahigh-strength MN–SI–Cr–C steel. *Mater. Sci. Eng. A* **2015**, *645*, 116–121. [CrossRef]

23. Zhao, P.; Gao, G.; Misra, R.; Bai, B. Effect of microstructure on the very high cycle fatigue behavior of a bainite/martensite multiphase steel. *Mater. Sci. Eng. A* **2015**, *630*, 1–7. [CrossRef]

24. Timokhina, I.; Hodgson, P.; Pereloma, E. Effect of microstructure on the stability of retained austenite in transformation-induced-plasticity steels. *Metall. Mater. Trans. A* **2004**, *35*, 2331–2341. [CrossRef]

25. Jiang, J.; Bao, W.; Peng, Z.; Wang, Y.; Liu, J.; Dai, X. Experimental investigation on mechanical behaviours of TMCP high strength steel. *Constr. Build. Mater.* **2019**, *200*, 664–680. [CrossRef]

26. Parthiban, R.; Chowdhury, S.G.; Harikumar, K.; Sankaran, S. Evolution of microstructure and its influence on tensile properties in thermo-mechanically controlled processed (TMCP) quench and partition (Q&P) steel. *Mater. Sci. Eng. A* **2017**, *705*, 376–384.

27. Kurpe, O.H.; Kukhar, V.V.; Klimov, E.S.; Prysiazhnyi, A.H. Thermomechanical controlled rolling of hot coils of steel grade S355MC at the wide-strip rolling mill 1700. *Solid State Phenom.* **2019**, *291*, 63–71. [CrossRef]

28. Haiko, O.; Miettunen, I.; Porter, D.; Ojala, N.; Ratia, V.; Heino, V.; Kemppainen, A. Effect of finish rolling and quench stop temperatures on impact-abrasive wear resistance of 0.35% carbon direct-quenched steel. *Tribol.-Finn. J. Tribol.* **2017**, *35*, 5–21.

29. Omale, J.; Ohaeri, E.; Szpunar, J.; Arafin, M.; Fateh, F. Microstructure and texture evolution in warm rolled API 5L X70 pipeline steel for sour service application. *Mater. Charact.* **2019**, *147*, 453–463. [CrossRef]

30. Saastamoinen, A.; Kaijalainen, A.; Porter, D.; Suikkanen, P.; Yang, J.-R.; Tsai, Y.-T. The effect of finish rolling temperature and tempering on the microstructure, mechanical properties and dislocation density of direct-quenched steel. *Mater. Charact.* **2018**, *139*, 1–10. [CrossRef]

31. Rui, S.-S.; Shang, Y.-B.; Su, Y.; Qiu, W.; Niu, L.-S.; Shi, H.-J.; Matsumoto, S.; Chuman, Y. EBSD analysis of cyclic load effect on final misorientation distribution of post-mortem low alloy steel: A new method for fatigue crack tip driving force prediction. *Int. J. Fatigue* **2018**, *113*, 264–276. [CrossRef]

32. Baek, M.-S.; Kim, K.-S.; Park, T.-W.; Ham, J.; Lee, K.-A. Quantitative phase analysis of martensite-bainite steel using EBSD and its microstructure, tensile and high-cycle fatigue behaviors. *Mater. Sci. Eng. A* **2020**, *785*, 139375. [CrossRef]

33. Keehan, E.; Karlsson, L.; Bhadeshia, H.K.D.H.; Thuvander, M. Electron backscattering diffraction study of coalesced bainite in high strength steel weld metals. *Mater. Sci. Technol.* **2008**, *24*, 1183–1188. [CrossRef]

34. Kang, S.; Yoon, S.; Lee, S.-J. Prediction of Bainite Start Temperature in Alloy Steels with Different Grain Sizes. *ISIJ Int.* **2014**, *54*, 997–999. [CrossRef]